Mesoporous silica nanoparticles functionalized with fluorescent and MRI reporters for the visualization of murine tumors overexpressing αvβ3 receptors

Mesoporous silica nanoparticles functionalized with fluorescent and MRI reporters for the visualization of murine tumors overexpressing $\alpha_v\beta_3$ receptors

He Hu, Francesca Arena, Eliana Gianolio, Cinzia Boffa, Enza Di Gregorio, Rachele Stefania, Laura Orio, Simona Baroni and Silvio Aime*

Corresponding author: Prof. Silvio Aime, email: silvio.aime@unito.it

Department of Molecular Biotechnologies and Health Sciences, University of Torino, Via Nizza, 52, TORINO, 10126, Italy. Tel: +39 0116706451, Fax: +39 0116706487.

Abstract:

A novel fluorescein/Gd-DOTAGA containing nanoprobe for tumor visualization by Optical and Magnetic Resonance Imaging (MRI) is reported. It is based on the functionalization of small mesoporous silica nanoparticles (MSNs) (~30 nm) surface with the arginine-glycine-aspartic (RGD) moieties which are known to target $\alpha_v\beta_3$ integrin receptors overexpressed in several tumor cells. The obtained nanoprobe (Gd-MSNs-RGD) displays good stability, tolerability and high relaxivity (37.6 $mM^{-1}s^{-1}$ at 21.5 MHz). After preliminary evaluation of the cytotoxicity and targeting capability toward U87MG cells by *in vitro* fluorescence and MR imaging, the nanoprobes were tested *in vivo* by acquiring T_1-weighted MR imaging of xenografted murine tumor models. The obtained results demonstrated that the Gd-MSNs-RGD nanoprobes are good reporters both *in vitro* and *in vivo*, for the MR-visualization of tumor cells overexpressing $\alpha_v\beta_3$ integrin receptors.

keywords: mesoporous silica nanoparticles, gadolinium complex, magnetic resonance imaging, high relaxivity, RGD

1 Introduction

Magnetic resonance imaging (MRI) has gained a primary position in diagnostic clinical medicine and biomedical research because it provides highly spatially resolved images of soft tissues without the need to use ionizing radiation.[1] In molecular imaging applications, MRI still suffers from a relatively low sensitivity of its probes, most of which are based on gadolinium complexes.[2] Therefore, the development of highly efficient contrast agents (CAs) is currently a topic of great interest in many laboratories. The efficiency of a paramagnetic CA is first of all described by its relaxivity (the relaxation enhancement of solvent water protons brought by the presence of the relaxation enhancer at 1 mM concentration), r_1, which depends on the structural, dynamic and electronic properties of the complex and its magnetic coupling with the solvent molecules.[3] According to the Solomon-Bloembergen-Morgan theory, the increase in relaxivity of a Gd-based CA can be pursued by several routes, i.e., a greater number of inner-sphere water molecules, *q*; an optimally short residence lifetime, τ_M, of the metal-coordinated water molecule(s); and a slow reorientational motion of the metal complex, τ_R.[2, 4] It was early shown that the latter task can be attained by immobilizing the Gd-CAs on nanostructured materials, thus slowing down their molecular tumbling but maintaining unaltered the water residence time. For example, nanomaterials, such as dendrimers,[5] polymers,[6-7] proteins,[8] gold [9] and silica[10-11] nanoparticles have been applied as slowly moving carriers for Gd(III)-complexes. One of the most significant limitation of the currently reported nanosized T_1-CAs is their large overall size (>100 nm) that markedly affect their *in vivo* distribution as they are quickly cleared by the reticuloendothelial system (RES). The RES is part of the immune system and consists of phagocytic cells like monocytes and macrophages that are located in the spleen, lymph nodes,

and liver Kupffer cells.[12] The large nanoparticles are readily cleared by RES or by the circulating mononuclear phagocytic system (MNP), while the smaller nanoparticles, particularly those smaller than 50 nm, exhibit longer retention time in the bloodstream and appear more suitable for pursuing their accumulation in diseased tissues.[13] For these reasons, there is still a great interest to develop MRI CAs based on small, monodisperse particles endowed with good stability and biocompatibility, site-specificity, and high relaxivity for *in vivo* imaging applications.

Mesoporous Silica Nanoparticles (MSNs) have been suggested as excellent candidate for building up an attractive multifunctional platform for diagnosis and therapy thanks to their peculiar properties such as high surface area, large pore volume, uniform and tunable pore size, and facile functionalization.[14] Currently, few MSNs-based agents have been proposed, whose main limitation appears associated to their overall large size and to their tendency to aggregate when dispersed in a physiological medium.[15] Although a recent report has shown that the size of MSNs can be reduced to be smaller than 50 nm, nevertheless, the obtained nanoparticles resulted to aggregate.[15-16] Therefore, a reliable large scale preparation of MSNs endowed with a small hydrodynamic diameter, functional groups and excellent dispersity in physiological aqueous conditions still remains challenging.

Cancer is a class of diseases in which a group of cells display uncontrolled growth, and ability to invade other tissues.[17] One of the hallmarks of the tumor progression is angiogenesis, *i.e.* the formation of new blood vessels, without which a tumor cannot grow beyond a few millimeters in diameter.[17] The cell adhesion receptor, integrin $\alpha_v\beta_3$, is an important player in the process of tumor angiogenesis and metastasis.[18] It's also a receptor for the extracellular matrix proteins that

owns an exposed cyclic arginine-glycine-aspartic (RGD) tripeptide sequence.[18] Therefore, the possibility of non-invasively imaging the integrin $\alpha_v\beta_3$ expression offers a route to diagnose cancer and its metastasis at an early stage of the tumor growth.[18-19] For this reason, probes conjugated with the RGD peptide have been suggested as efficient systems for targeting integrin $\alpha_v\beta_3$ receptors.[20]

In this work, we report the design and testing of a high r_1-relaxivity, bimodal (Optical and MRI) targeting nanoprobe based on a multifunctional platform of fluorescein-doped and amino-functionalized, small sized MSNs. The macrocyclic Gd-DOTAGA [DOTAGA=2-(R)-2-(4,7,10-triscarboxymethyl-1,4,7,10-tetra-azacyc -lododec-1-yl) pentanedioic acid], which features four carboxylate donor groups and one inner-sphere water molecule, was used as MRI reporter (Scheme 1). The paramagnetic Gd-MSNs were further labeled with RGD peptides to target integrin $\alpha_v\beta_3$ receptors. The cytotoxicity and targeting capability of the obtained multifunctional nanoprobes were first evaluated *in vitro*, in U87MG human glioblastoma cell line, and then further validated *in vivo* for targeted T_1-weighted MR imaging of a xenografted tumor model.

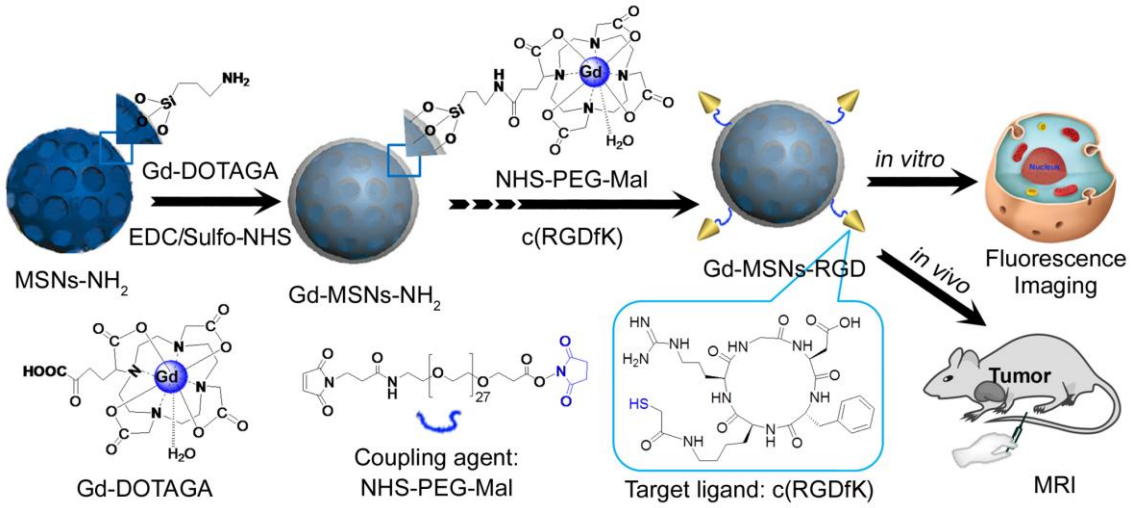

Scheme 1. The synthetic route of the FITC-doped MSNs-NH_2, followed by Gd-DOTAGA and RGD-conjugation for bio-applications.

2 Results and discussion

2.1 Synthesis and characterization of the multi-functionalized Gd-MSNs-RGD nanoprobe: As a general rule, large nanoparticles are preferentially filtered out by RES, whereas tiny nanoparticles tend to be cleared through kidneys.[21] Therefore, it has been suggested that nanoparticles within the size of 10 ~ 50 nm in diameter are greatly desirable for *in vivo* applications.[22-23] Common synthetic strategies for functionalized MSNs invariantly result in irreversible and extensive nanoparticle aggregation during the surfactant removal and post-functionalization processes.[22] Poly(ethylene glycol)-silane (PEG-silane) has been widely used to control the MSNs size by terminating the silica condensation on the nanoparticle surface.[16, 24] In the herein proposed procedure, a PEG-silane free, one-pot, soft-templating sol-gel technique was adopted to fabricate the fluorescein-doped and amino-functionalized MSNs (MSNs-NH_2) by using cetyl-trimethylammonium bromide (CTAB) as the templating surfactant and triethanolamine (TEAH3) as the mineralizing agent under mild conditions. High quality MSN-NH_2were produced at grams-scale with an overall high yield of 98 %. The size and morphology of the MSNs were assessed by transmission electron microscopy (TEM) as shown in Figure 1. The MSNs-NH_2 display high monodispersity and narrow size distribution around 30 nm as shown in the low magnification TEM image (Figure 1a). The high magnification TEM image showed that the obtained MSNs were characterized by a spherical raspberry morphology with a well-defined structure (Figure 1b). The stock aqueous suspension of the amino functionalized MSNs (MSNs-NH_2) appears very stable as transparent colloidal

solution, at concentration of 10 mg/mL in 100 mL bottle, is maintained over a long time (2-3 months). By exposing the suspension to the light of an intense red laser path, the classical Tyndall effect of the colloidal solution was clearly observed (Figure 1c). MSN-NH_2 were then further conjugated with Gd-DOTAGA, PEG_{1570} and the targeting ligands RGD, to yield the Gd-MSN-RGD that did not display any significant change in morphology or size as witnessed by the TEM observation (Figure 1e-f). The surface modification procedure has no negative effect on the solubility of the final product which exhibited strong green fluorescence under excitation of a portable UV (365 nm) (Figure 1d). To get more insight into the stability of the obtained MSNs in physiological conditions, the hydrodynamic diameters of the MSNs were monitored in phosphate-buffered saline (PBS) solution (pH 7.4) over a period of two months by dynamic light scattering (DLS) measurements (Figure 1g). The average hydrodynamic diameter (assessed on the basis of the intensity of the scattered light) of the MSN-NH_2 resulted stable at 33±2 nm (with a mean poly-dispersity index (PDI) of 0.028±0.003) which is slightly larger than the value obtained by TEM. This discrepancy is attributed to the hydration sphere of the nanoparticles in solution. The mean hydrodynamic diameter of the functionalized Gd-MSN-RGD increased to 43±3 nm (PDI 0.077±0.004) due to the protruding of the surface ligands in solution.

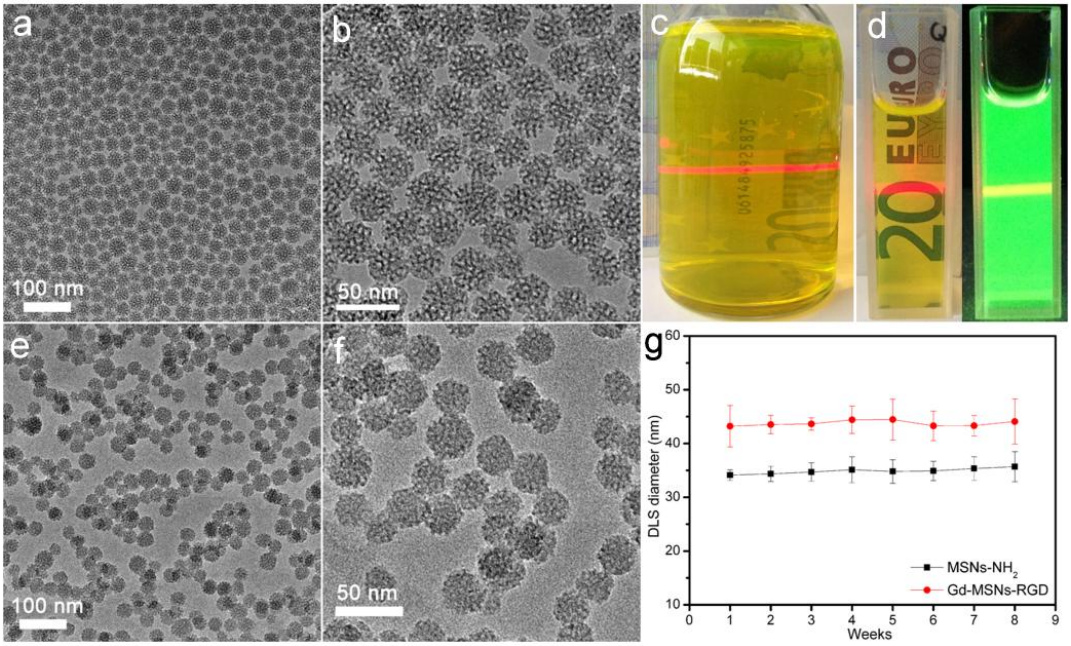

Figure 1. Low magnification TEM images of (a) FITC-doped MSNs-NH_2 and (e) Gd-MSN-RGD, high magnification TEM images of (b) FITC-doped MSNs-NH_2 and (f) Gd-MSN-RGD. The photographs demonstrate the clearly transparent colloidal solution of (c) FITC-doped MSNs-NH_2 (10 mg/mL) and (d) Gd-MSN-RGD (3 mg/mL) and it's corresponding fluorescence under a portable UV lamp (365 nm) excitation. (g) Long-term colloidal stability of the FITC-doped MSNs-NH_2 and Gd-MSN-RGD in PBS (pH 7.4, 25 ^{o}C), reported as variation of the mean hydrodynamic diameter obtained by DLS size distribution (assessed by means of the measured intensities). The error bars were obtained from three independent measurements.

Based on the DLS measurements, both MSN-NH_2 and Gd-MSN-RGD displayed a very good monodispersity. No significant size change was observed after storage for 8 weeks demonstrating their good colloidal stability in PBS. The surface area and the pore structures of the MSNs were characterized by the well-established N_2 adsorption-desorption technique as shown in Figure 2. The isotherms of both the samples exhibit the Langmuir IV type hysteresis which indicates the presence of well-defined mesoporous structures (Figure 2a). Calculated on the basis of the Brunauer-Emmett-Teller (BET) method, the surface areas of MSN-NH_2 and

Gd-MSN-RGD resulted to be 442 m^2/g and 237 m^2/g, and the pore volumes of these two samples were 1.01 and 0.92 cm^3/g, respectively. By nonlocal density functional theory (NLDFT) calculations with the spherical-pore model,[25] a uniform pore size distribution centered at 4.5 nm and 3.7 nm can be obtained for the MSN-NH_2 and Gd-MSN-RGD, respectively (Figure 2b). We found that upon functionalizing with RGD, the surface area, pore volume and size of the resulting nanoparticles were smaller than those found for the parent MSN-NH_2 materials. Notably, the Gd-MSN-RGD still displayed a quite large surface area (237 m^2/g) that will allow a good drug payload for future "theranostic" applications.

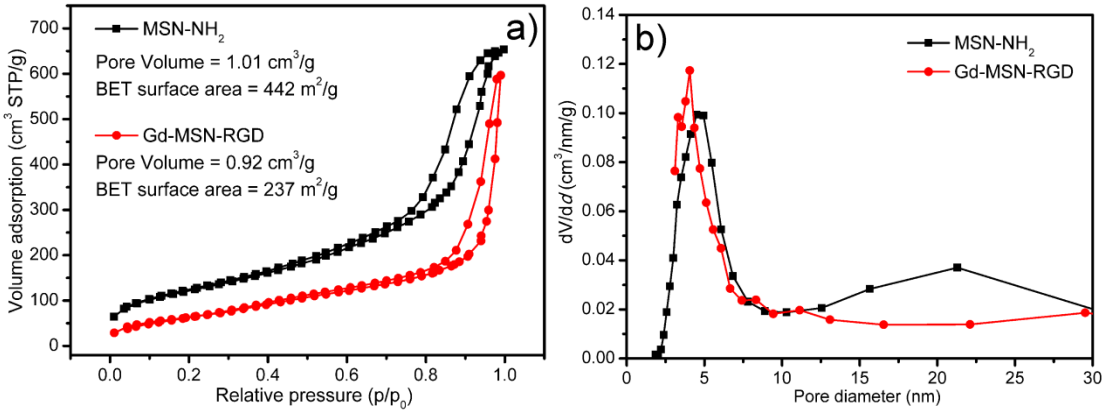

Figure 2. N_2 adsorption-desorption isotherms (a) and the corresponding pore size distribution (b) of MSNs-NH_2 (■) and Gd-MSN-RGD (●), respectively.

The room-temperature absorption and emission spectrum of Gd-MSN-RGD in aqueous solution showed the characteristic optical properties of fluorescein (Figure S1, supporting information). The intense fluorescence emission clearly indicated that these particles can be detected in fluorescence imaging. The successful surface modification of the MSNs was confirmed by the following characterizations. (1) In TEM images, composition analyses by energy dispersive X-ray (EDX) (Figure S2) and X-Ray photoelectron spectrometry (XPS) (Figure S3) revealed the presence of large amounts of Gd and a great increase of C and O in the

Gd-MSNs-RGD specimen, supporting the occurrence of a successful functionalization (Figure S2). (2) Both Fourier transform infrared (FTIR) spectroscopy and thermogravimetric analysis (TGA), before and after bio-conjugation (see Supporting Information for a detailed explanation - Figure S4 and S5), were investigated. The strong and broad band in the range of 1207 ~1047 $cm^{-1}$and a relative weak peak at 460 cm^{-1}, correspond to the Si-O-Si asymmetric (ν_{as}) stretching vibrations arising from the SiO_2 matrix. Upon reaction wtih Gd^{3+}-DOTAGA, PEG and RGD, new peaks (at ν =1546 and 1627 cm^{-1}) are observed which can be attributed to the vibration of imide-bond (Figure S3B). Moreover, the sharp peak at 1089 cm^{-1} belongs to the C-O-C stretching vibration from the PEG chains. The bioconjugation also caused 19 % increase of weight in the TGA data, giving support to the accomplishment of surface modification.(3) The surface zeta-potential of MSNs-NH_2 was +25.4 mV in PBS buffer at neutral pH. After the introduction of the negatively charged Gd-DOTAGA complexes and PEG, the value decreased to -25.6 mV. The further conjugation with RGD peptides, caused only a minor change in the zeta potential value (-23.4 mV) consistent with the introduction of about 60 μmol/g of RGD on the outer surface of the MSNs (Figure S6). (4) The amount of the amine-groups on the surface of MSNs-NH_2 was identified to be 420 μmol/g (~ 2.5 -NH_2 per nm^2) by using a Fmoc-Cl quantification protocol.[26] After conjugation with Gd-DOTAGA complexes, about 25 % of free amine-groups (105 μmol/g or 0.6 -NH_2 per nm^2) resulted available on the surface of Gd-MSNs-NH_2 (with ~ 1.9 Gd^{3+} per nm^2) for the reaction with PEG and RGD peptides. The amount of amines in the final Gd-MSNs-RGD product (with ~ 0.4 RGD molecules per nm^2) was below the detection limit to indicate a good extent of conjugated PEG and RGD moieties (The calculation process was demonstrated in supporting information).

2.2 Relaxation enhancement of the Gd-MSNs-RGD nanoprobe: The longitudinal proton relaxivity, r_1, is the measure of the efficacy of the paramagnetic complex in accelerating the relaxation rate of water protons. This fundamental parameter, that characterizes the properties of a positive MRI contrast agent, is calculated from the observed Relaxation rate constant, R_{1obs}, by subtracting the diamagnetic contribution, R_{1d}, and dividing by the actual concentration of Gd^{3+} ions. R_{1d} is the relaxation rate of an identical solution without the paramagnetic ions, and in our case coincides with the value measured for an aqueous suspension of the neat MSNs (0.37 s^{-1} at 21.5 MHz, 25 ^{o}C).

The transverse (R_2) and longitudinal (R_1) relaxation rates ($R_i=1/T_i$) of water protons as a function of Gd^{3+} concentration for Gd-MSNs-RGD have been measured at the fixed Larmor frequency of 21.5 MHz and at 25 ^{o}C. As shown in Figure 3a, the r_1 and r_2 values (slopes of the lines) resulted to be 37.4 and 47.2 $mM^{-1}s^{-1}$, respectively. The r_1 value is ca. 7-times higher than that of the commercial T_1 MRI contrast agents (3 - 5 $mM^{-1}s^{-1}$). The efficacy of contrast agents to be used as positive T_1 agents is also governed by the ratio of r_2/r_1, and low r_2/r_1 ratios are considered to be ideal. The r_2/r_1 ratio of Gd-MSNs-RGD is 1.26 indicating that the MSNs obtained in this work could act as very efficient T_1-enhancers. The high sensitivity is a primary requirement for molecular imaging applications as the targeting receptors are present at very low concentration. The T_1-weighted MR-Image of a phantom of Gd-MSNs-RGD aqueous solutions with different Gd^{3+} concentrations was carried out on a 1-T MRI Scanner as shown in Figure 3b. Upon increasing the Gd^{3+}concentration from 0 to 540 μM, the images gradually became brighter.

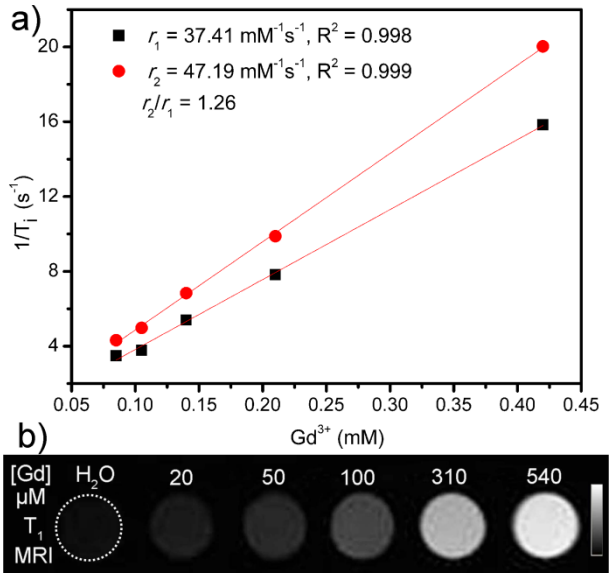

Figure 3. a) Water proton longitudinal (R_1) and transversal (R_2) relaxation rates of Gd-MSNs-RGD as a function of Gd^{3+} concentration measured at 21.5 MHz and 25°C. b) T_1-weighted MR images of Gd-MSN-RGD aqueous solutions at various concentrations of Gd^{3+} (the black and white bar changing from black to white indicates the gradual increased in MR signal) obtained from 1-T MRI scanner.

In table 1, sizes and longitudinal relaxivities of recently reported analogously functionalized nanoparticles are reported. The herein reported Gd-MSNs resulted to be among the most efficient systems when compared to analogue structures under similar conditions.

Table 1. Comparison of longitudinal relaxivities of different Gd-complex conjugated nanoparticles

Compounds	size (nm)	r_1 ($mM^{-1}s^{-1}$)	field (MHz)	Cell or in vivo	Target	ref.
Gd(DOTAGA)-MSN	30	28/37	60/20	Both	Yes	This work
Gd(DOTAGA)-MSN	25-220	20.3-79.1	20	No	No	3, 10
Gd(DOTA)-Dendrimer	142	22.4	60	in vivo	No	5
Gd(DOTA)-PLGA	150 -170	17.5	60	No	No	6
Gd(DOTA)-PLGA	140	21.7	21.5	in vivo	No	7
Gd(DOTA)-TWV	260 -640	14.6	60	in vivo	Yes	8
Gd(DTPA)-PLNP	109	6.72	50	in vivo	No	27

Gd(HPDO3A)-PN		17	60	in vivo	No	28
Gd(DTPA)DNA-Au	30	20	60	cell	No	9
Gd(DOTA)-MSN	20-50	26.6	20	No	No	3
Gd(DTPA)-MSNR	107-535	22	20	cell	No	11

TWV: tobacco mosaic virus, PLNP: persistent luminescent nanoparticles; PN: peptide nanofiber; MSN: mesoporous silica nanoparticles; PLGA: poly(D,L-lactide-co-glycolide); The molecular structures of the Gd-complex are shown in Figure S7.

It was recently demonstrated, that the chemical nature of the surface of functionalized MSNs affects the relaxometric properties of the conjugated Gd-complexes.[3, 10] In particular, the presence of pendant amino groups, which are protonated at neutral pH, can affect the water exchange rate of the Gd-coordinated water molecule by establishing an electrostatic interaction with the negatively charged Gd-DOTAGA complexes. The overall result is the decrease of the residual negative charge that, in turn, yields a "quenching" of the relaxivity of the paramagnetic complex. The relaxivities of the herein synthetized Gd-MSNs-PEG and Gd-MSNs-RGD, on the contrary, seem not to be affected by the presence of free amino groups, as their values are higher than that previously reported for analogous NH_2 functionalized MSNs (20.3 $mM^{-1}s^{-1}$ at 20 MHz and 310 K) and very close to that observed upon transformation of the amino functionalities into neutral amide groups (37.8 $mM^{-1}s^{-1}$ at 20 MHz and 310 K).[10] Likely, the observed behavior has to be accounted for the considerably lower density of -NH_2 functionalization of the MSNs presented in our work (<0.1 mmol/g) with respect to that of the MSNs reported in reference 3 and 10 (2.8 mmol/g).

For a thorough relaxometric characterization of the two probes, the nuclear magnetic relaxation dispersion (NMRD) profiles of Gd-MSNs-PEG and Gd-MSNs-RGD were measured over the frequency range of 0.1 – 70 MHz at 25 ^{o}C (Figure 4). The NMRD profiles of the two

probes were almost identical with a relaxivity peak centered on 21 MHz, typical of slowly tumbling systems. The experimental data were fitted to the Solomon–Bloembergen–Morgan equations (4 – 70 MHz), modified by incorporating the Lipari–Szabo approach for a better definition of the rotational dynamics (Table 2), *i.e.* the spectral density function is governed by two terms: one is related to the global motion of the nanoparticles (τ_{RG}) and the other to the local rotation of the complex around the axis of the linker (τ_{Rl}), respectively. The obtained correlation times are related by the factor S^2 ($0 \leq S^2 \leq 1$) which describes the degree of spatial restriction: if the motion of the Gd-complex is totally independent from that of the nanoparticle, $S^2 = 0$, while if the Gd complex is completely immobilized on the nanoparticles, then $S^2 = 1$. Considering the slow global tumbling of the nanosized systems, the τ_{RG} was fixed to 100 s.[10] The small S^2 (0.354 and 0.346) and short τ_{Rl} (1.17 and 0.992 ns) values indicated the occurrence of a high degree of local mobility. By assuming that the exchange with the bulk solvent is not significantly affected by the structural constrain resulting from the conjugation of the metal complex to the MSNs surface, data were fitted by fixing the residence lifetime of the coordinated water (τ_M) to that of the parent Gd-DOTA complex (0.24 μs).[29]

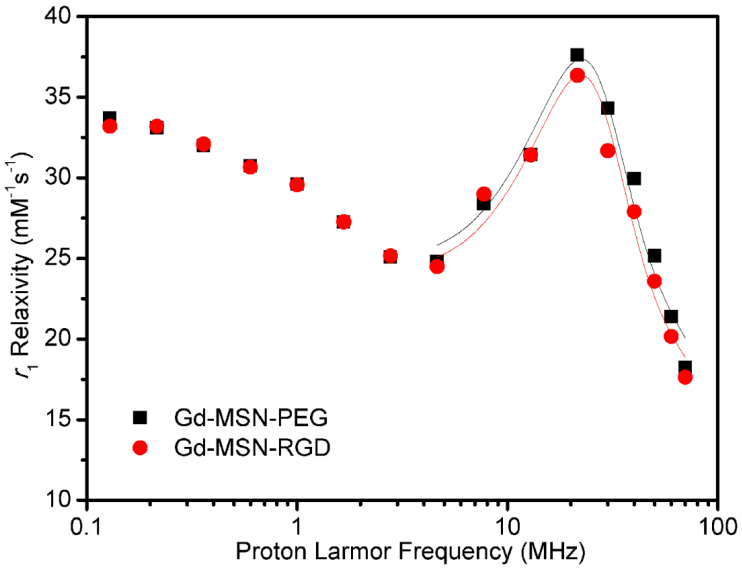

Figure 4. The magnetic-field dependence of the relaxivity (r_1) measured over an extended range of magnetic field strengths (from 0.01 to 70 MHz). The nuclear magnetic relaxation dispersion (NMRD) profiles were obtained for the aqueous suspensions of Gd-MSN-RGD(■) and Gd-MSNs-PEG (●) at 25 ^{o}C and normalized to 1mM concentration of Gd^{3+}.

Table 2. Summary of the best-fitting values of key parameters obtained from the analysis of NMRD profiles reported in Figure 4.[a]

Compounds	r_1 **(mM^{-1}s^{-1})**	τ_{RG} **(ms)***	τ_{RI} **(ns)**	τ_M **(μs)***	S^2
Gd-MSNs-RGD	37.60	0.1	1.17	0.24	0.354
Gd-MSNs-PEG	36.33	0.1	0.992	0.24	0.346

[a] The distance of the proton of the coordinated water molecule from the metal ion (r_{Gd-H}) was fixed to 3.0 Å. * These values were kept fixed during the fitting procedure.

2.3 Cytotoxicity and cell imaging: The *in vitro* cytotoxicity of Gd-MSNs-RGD was assessed on U87MG cells by using the Cell Titer-Blue® cell viability Assay (Figure 5). The viability of the untreated cells was used as the control (100 %). No significant decrease in the cell viability (> 93%) was observed upon incubating the U87MG cells with Gd-MSNs-RGD (concentration: 100 to 800 μg/mL) at 37 ^{o}C for 6, 12 or 24 h. Notably, the cell viability was still higher than 90 % even after 24 h incubation with 800 μg/mL of the probes, a dose which is much higher than that used for *in vitro* and *in vivo* applications.

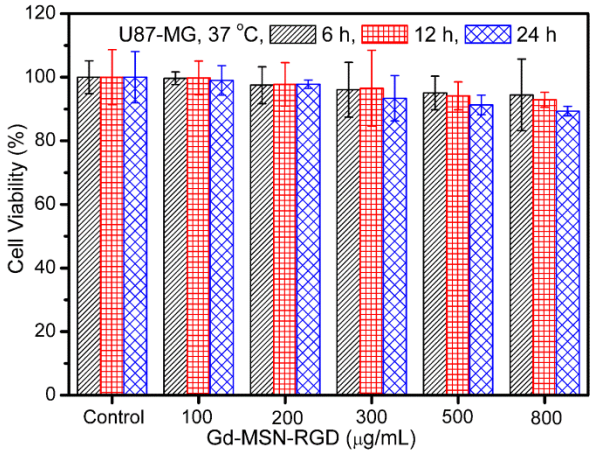

Figure 5. Cell viability of a human glioblastoma U87MG cell line incubated with different concentrations of Gd-MSNs-RGD for 6, 12 and 24 h, respectively.

The integrin $\alpha_v\beta_3$ binding affinity of RGD-conjugated MSNs was first evaluated by laser confocal scanning microscopy (LCSM) (Figure 6). An intense green fluorescence signal was observed on the integrin-positive U87MG cells upon applying the 488 nm laser excitation. To establish the localization of nanoprobes, the nuclei of the U87MG cells were stained with the blue fluorescent dye DAPI. The image overlaying FITC and DAPI emissions shows that Gd-MSNs-RGD distributes either at the cell surface and inside the cells, likely internalized into endosomes as it is well established that these receptors undergo receptor-mediated endocytosis.[18] For comparison, the control experiment of CLSM imaging was carried out by incubating Gd-MSNs-PEG (no RGD ligands) with U87MG cells under identical conditions. Negligible signals were detected at the U87MG cells due to the lack of specific integrin $\alpha_v\beta_3$ targeting ligands. In addition, binding of the nanoprobes to U87MG cells was effectively blocked in presence of 2 μM free RGD before the incubation with Gd-MSNs-RGD. Only a very weak fluorescence could be detected which is ascribed to the passive uptake of nanoparticles.

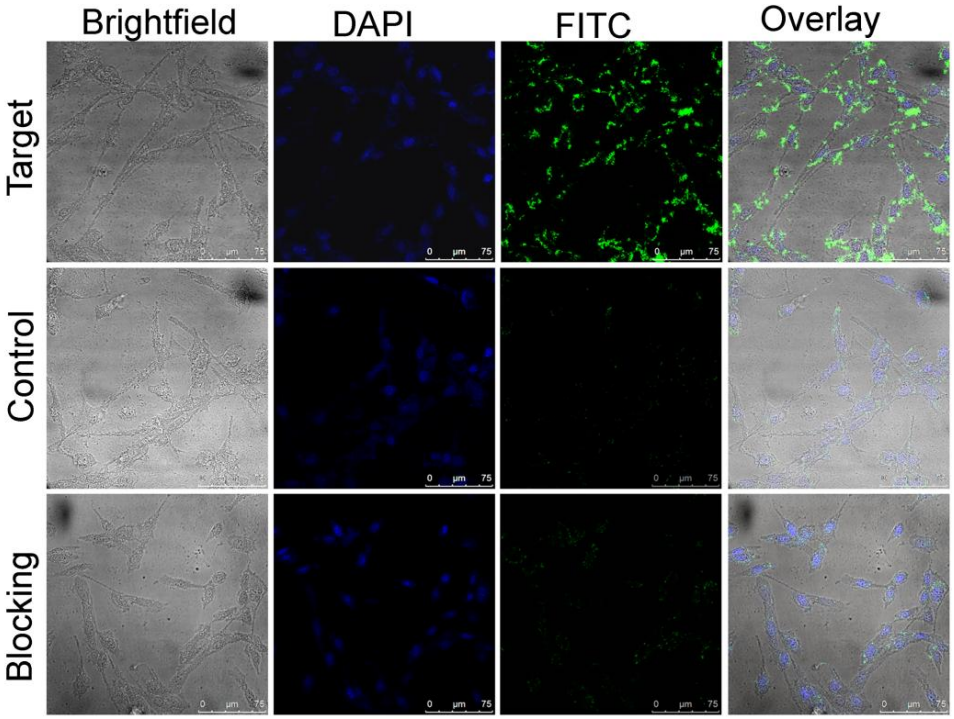

Figure 6. Confocal laser scanning microscopy (CLSM) images of U87MG cells incubated with Gd-MSNs-RGD (target group) and Gd-MSNs-PEG (control group) at 200 μg/mL concentration at 37 ^{o}C for 4 h (scale bar = 75 mm). The blocking experiment was carried out by incubating U87-MG cells with Gd-MSNs-RGD in the presence of an excess of free RGD (2 μM).

Furthermore, to evaluate the feasibility of using the Gd-MSNs-RGD nanoprobes to detect cancer cells by MR imaging, the MR signal intensity of U87MG cells incubated with both Gd-MSNs-PEG (as control RGD-) and Gd-MSNs-RGD (as target RGD+) at different Gd concentrations (0, 5, 10, 15, and 20 μM) were acquired on a 7T MRI scanner (Figure 7a). The Gd-MSNs-RGD highlighted the U87MG cells upon increasing Gd concentration. The MR signal enhancement is much greater than that of the control group. The amount of Gd uptaken by U87MG cells was quantified by inductively coupled plasma–mass spectrometry (ICP-MS) and Bradford protein assay (Figure 7b). The amount of Gd^{3+} uptaken in targeted cells is 0.92, 1.4, 2.8, and 4.4 nmol Gd^{3+} per mg of protein, respectively. Whereas, the Gd^{3+} uptake in control

group was much lower as 0.15, 0.31, 0.63, and 1.4 nmol Gd^{3+} per mg of protein were measured, respectively. At low particle's concentrations, the uptake from targeted group is 6 fold higher than that of the control group. αvβ3 receptors are known to internalize quite efficiently RGD-functionalized substrates, thus, we surmise that most of the RGD-functionalized MSNs have been internalized by receptor-mediated endocytosis. From both fluorescence and MRI cell-staining experiments, it can be concluded that Gd-MSNs-RGD exhibits a good integrin $\alpha_v\beta_3$-specific binding capability *in vitro*.

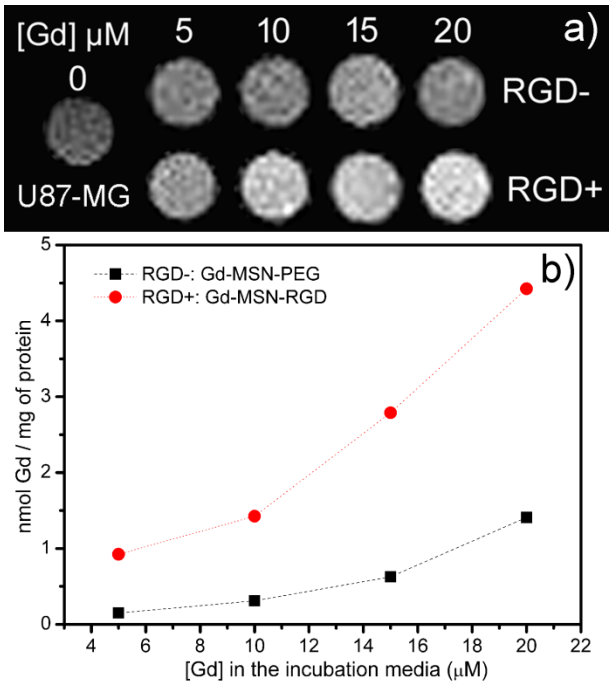

Figure 7. a) T_1-weighted MR images (at 7T) of U87MG cells incubated with Gd-MSNs-PEG and Gd-MSN-RGD for 3 h at 37 °C. b) Results of the quantitative analysis of Gd^{3+} entrapped into the U87MG cells measured by ICP-MS and Bradford protein assay after MR imaging.

2.4 Targeted *in vivo* MR imaging and ex vivo biodistribution studies:

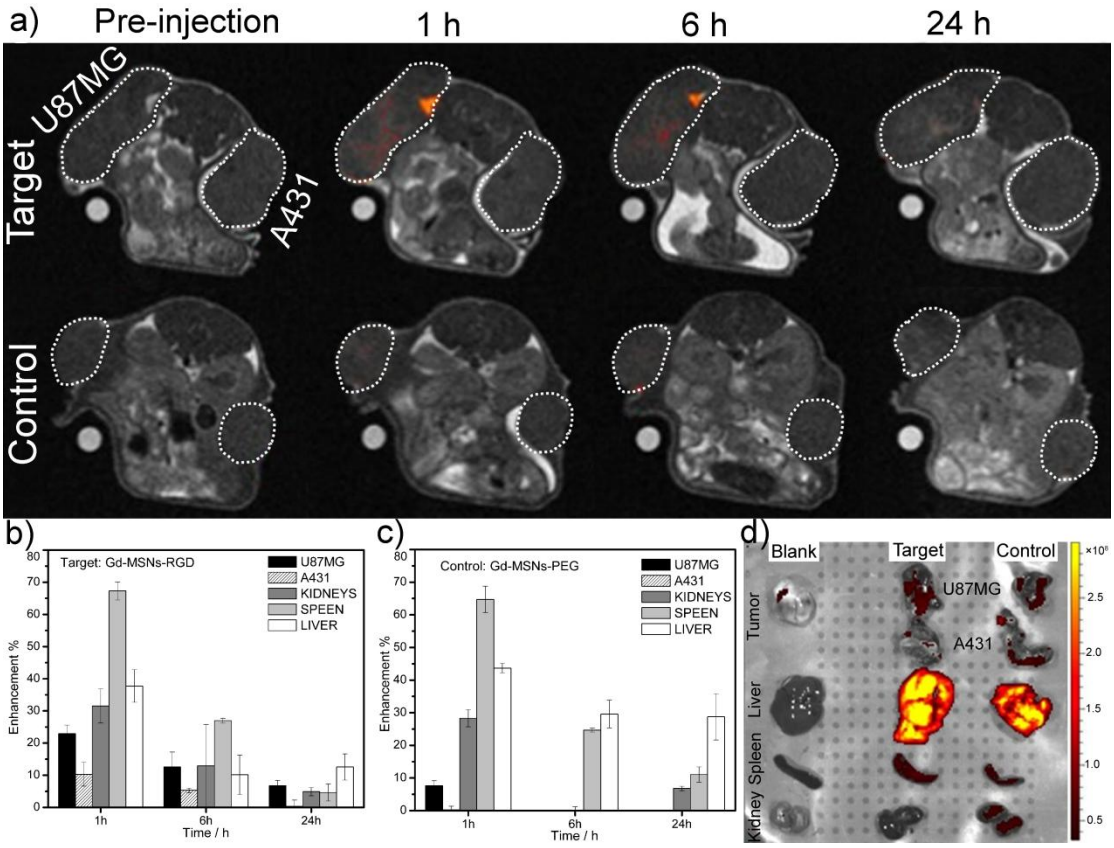

Figure 8. a) *In vivo* T_1-weighted MR images of subcutaneous U87MG glioblastoma (over expressing $\alpha_v\beta_3$) and A431 (low expressing $\alpha_v\beta_3$) tumor-bearing athymic nude mice (n = 3) obtained before and after 1h, 6h and 24 h the intravenous injection of Gd-MSN-RGD (target group) and Gd-MSNs-PEG(control group). The red spots correspond to the signal enhanced pixels. Quantitative analysis of signal intensity enchantment of b) target group and c) control group MR images. d) Ex vivo fluorescence images of main organs resected after completion the MRI scanning (24 h post-injection).

The *in vivo* targeting capability of Gd-MSNs-RGD towards $\alpha_v\beta_3$ integrin receptors has been assessed by acquiring signal intensity enhancements in T_1-weigthed MR imaging at different time points (1, 6 and 24 h) post injection. Athymic nude mice (*n* = 3) bearing two xenografted tumors were used, namely the human malignant glioma U87MG on the left shoulder ($\alpha_v\beta_3$ overexpressing tumor) and the human epidermal carcinoma A431 on the right shoulder (as

control), respectively. The Gd-MSNs-RGD were used as targeting nanoprobes while Gd-MSNs-PEG (without RGD vectors) were used as control probes. The T_1-weighted MR images of U87MG tumor showed significant signal enhancements as compared with the images of A431 tumor upon tail vein administration of Gd-MSNs-RGD (at the dose of 0.021 mmol/kg) after 1 and 6 h (Figure 8a). The fast accumulation of the targeting nanoprobes at the U87MG tumor site could be attributed to their small size. The signal to noise enhancement of the T_1-MR image in U87MG tumor was about 2.3 times higher than that in A431 tumor (Figure 8b). At 24 h time point, the signal enhancement in U87MG tumor was decreased and this may be due to the biodegradation and clearance of the nanoprobes from the body. The targeting specificity was further checked, by using Gd-MSNs-PEG (i.e. without RGD ligands) as negative control. In this experiment, nearly no contrast enhancement in both tumors was observed. These results indicated that the Gd-MSNs-RGD nanoprobes display an efficient active targeting ability towards the integrin $\alpha_v\beta_3$ receptors overexpressed in U87MG tumor. A relatively large amount of nanoprobes accumulates in liver and spleen, with both targeted and control probes. The accumulation in liver and spleen is expected for nanoparticles, which are taken up from circulation mainly through the RES. It should be noted that the wash-out of the targeted nanoprobes in these organs was not as fast as that in the control group (Figure 8b-c). This could be caused by the normal expression of $\alpha_v\beta_3$ integrin in these organs according to previous reports.[18, 20] To double confirm the imaging results and trace the biodistribution of the nanoprobes in mice, the *ex vivo* fluorescence images of major organs (tumor, liver, spleen, kidney,) were examined using fluorescence microscopy (Figure 8d). Similar to the *in vivo* images, significant intensive emissions from the nanoprobes were observed in U87MG tumor of

the targeted group, suggesting highly efficient targeting ability of the Gd-MSNs-RGD. Collectively, the above observations demonstrated that the Gd-MSNs-RGD could be used as a positive MRI contrast agents for *in vivo* imaging applications.

3 Experimental

3.1 Materials: Chemicals and materials:1-ethyl-3-(3-dimethylaminopropyl) carbodiimide hydrochloride salt (EDC), *N*-hydroxysulfosuccinimide (Sulfo-NHS), fluorescein-5-isothiocyanate (FITC), (3-Aminopropyl)trimethoxysilane (APTES), hexadecyltrimethyl-ammonium bromide (CTAB), triethanolamine (TEAH3), O-[*N*-(3-Maleimidopropionyl)-aminoethyl]-O′-[3-(*N*- succinimi-dyloxy)-3-oxopropyl] heptacosaethylene glycol ≥ 90% (Mal-PEG_{27}-NHS ester), Dimethylformamide (DMF), dimethyl sulfoxide (DMSO) and all the solvents were purchased from Sigma−Aldrich and used without further purification. 4′,6-diamidino-2- phenylindole (DAPI) was purchased from Life Technologies, Inc. The cyclic 5mer cyclo(-Arg-Gly-Asp-d-Phe-Lys-) (c(RGDfK)) peptide with the thioether group at the lysine residue was purchased from CS Bio Co. 2-(R)-2-(4,7,10-triscarboxy-methyl-1,4,7,10-tetraazacyclododec-1-yl) pentanedioic acid = DOTAGA was synthesized, as reported previously.[30] Water used in all experiments was purified using a Milli-Q Plus 185 water purification system (Millipore, Bedford, MA) with resistivity higher than 18 MΩcm.

3.2 Synthesis of FITC-doped and amino-functionalized small size MSNs (MSNs-NH_2): The The synthesis of FITC-doped MSNs-NH_2 has been carried out according to a slight modification of a previous report.[31]

Firstly, 12 mg of FITC were conjugated to APTES (2 mL in 1 mL dried DMF). The mixture was stirred overnight under dark to yield FITC-silane in APTES solution (the obtained molar

ratio of FITC-silane to APTES is 1: 370). Then, a mixture of 2.1 mmol of CTAB, 0.91 mmol of TEAH3 and 100 mL of deionized water was stirred at 80 ^{o}C for 1 hour, and 4 mL of TEOS was quickly added into the surfactant solution and stirred at 12000 rmp for 30 min. Then, 1.5 mmol of FITC-silane in APTES was added dropwise and the reaction was stirred at 60 °C for other 3.5 h. Afterwards, the reaction solution was cooled to room temperature (R.T.) and then transferred into a dialysis membrane tube (Pierce, Molecular Weight Cut Off 10,000) where it was dialyzed in 500 ml acid solution composed by water, ethanol and acetic acid (volume ratio 1:1:0.01) for 24 h to extract CTAB out of the pores of the silica nanoparticles. This process was repeated three times. The solution was then dialyzed in 2 L D.I.-water for 4 h. This process was repeated two times. The final colloidal product was collected and concentrated by evaporating water at room temperature (98 % yield). The reaction volume of this protocol can be varied from 10 mL to several hundred milliliters according to the output requirement.

3.3 Functionalization of MSNs-NH_2 with Gd-DOTAGA and RGD ligands (Gd-MSNs-RGD): Firstly, the free carboxyl group of Gd-DOTAGA complex was activated with EDC and Sulfo-NHS (with a molar ratio of -COOH/EDC/Sulfo-NHS = 1:5:8) at R.T. for 4 h. Then, 20 mg of MSNs-NH_2 (10.2 μmol in terms of -NH_2 groups) in 3 mL DMSO solution were added into the activated Gd-DOTAGA solution (with a molar ratio of -NH_2/-COOH = 1:3), the mixture was stirred for 6 h at R.T. The product was transferred into a dialysis membrane tube and dialyzed against 1 L of water for 3 times and dispersed in 2 mL of PBS after being concentrated by ultrafiltration spin columns (Vivaspin, Molecular Weight Cut Off 10,000). Subsequently, 1 mmol of Mal-PEG-NHS was added into the above PBS solution and stirred for 2 h at R.T., then, 2 mmol of thiolated c(RGDfK) peptide was added and stirred for 4

h. For the nanoprobes used as control (Gd-MSNs-PEG), an excess of ethanethiol (instead of RGD) was added to the solution to block the maleimide group of PEG. The final product was purified by dialysis in water, concentrated and stored in 2 mL PBS solution for further use.

3.4 Particles characterization： Size and morphology of the MSNs were observed by a JEOL-2100 transmission electron microscope (TEM) equipped with the energy-dispersive X-ray spectrum. Fourier transform infrared (FTIR) spectra were performed using a Nicolet Avatar 370 with KBr pellets. The X-Ray photoelectron Spectromete (XPS) experiments were carried out on a RBD upgraded PHI-5000C ESCA system (Perkin Elmer) with Al Kα radiation (hν = 1486.6 eV). The amount of surfactant present on the surface of MSNs was quantitatively measured by thermogravimetric analysis (TGA) curves which were recorded on a DTG-60H (Shimadzu) at a heating rate of 10 ^{o}C/min. The UV-vis spectra and fluorescence spectra were recorded by using the Olis Globalworks Cary 14 UV–vis absorption spectrophotometer and HORIBA Nanolog fluorimeter, respectively. The hydrated mean diameter and surface potential of the MSNs samples were determined by means of dynamic light scattering (DLS) Malvern Zetasizer 3000HS (Malvern, U.K.).

3.5 Relaxivity measurements and *in vitro* MRI of Gd-MSNs-RGD aqueous suspensions： The Proton Nuclear Magnetic Relaxation Dispersion (NMRD) $1/T_1$ Profiles data were measured at 25 °C over a continuum of magnetic field strengths from 0.00024 to 0.47 T (corresponding to 0.01-20 MHz proton Larmor Frequency) on a Stelar field-cycling relaxometer (Stelar, Mede, Italy), under complete computer control with an absolute uncertainty less than 1%. Data points from 0.5 T (21.5 MHz) to 1.7 T (70 MHz) were collected on a Spinmaster spectrometer (Stelar, Mede, Italy) working at variable fields. The concentration of Gd^{3+} of the samples was

determined by the following protocol: 100 μL of the samples were treated with 100 μL HCl 37 % in sealed vials at 120 °C overnight in order to destroy the Gd-complexes and obtain Gd^{3+} aqua-ion. The R_1 of these solutions was measured at 21.5 MHz and 25 °C. The Gd^{3+} concentration was calculated from a calibration curve obtained by using standard solutions of $GdCl_3$.[32]

MR images of the phantom of Gd-MSNs-RGD aqueous solutions at different Gd^{3+} concentrations (0 ~ 540 μM) were acquired on Aspect M2-High Performance 1T MRI Scanner (Aspect Imaging, Israel) by using a T_1-weighted Spin-Echo imaging protocol (TR/TE/NEX =100:13:12; FOV = 24mm).

3.6 Cell culture and cytotoxicity test：U87MG cell line is a glioblastoma, astrocytoma cell line derived from human malignant gliomas. U87MG cells were cultured by growing cells in EMEM (Euroclone-Lonza) + 10% fetal bovine serum (Euroclone-Lonza) + 100 units/ml penicillin +100 μg/ml streptomycin + 2mM Glutamine + 1% Non Essential Amino Acids (NEAA) + 1mM Sodium Pyruvate (NaP) + 5% CO_2 at 37 ^oC. The cell viability was assessed by standard CellTiter-Blue® Cell Viability Assay Protocol. 5×10^4 cells/well was seeded into 96-well assay plates in culture medium. The cells were incubated with Gd-MSNs-RGD with different concentrations (0, 100, 200, 300, 500 and 800 μg/mL) for 6, 12 and 24 h at 37 ^oC under 5 % CO_2. To minimize the test error, each concentration at each time point was measured in triplicate. Wells without cells were used as the negative control to determine background fluorescence. Thereafter, 20 μL/well of Cell Titer-Blue® Reagent were added and the final volume brought to 120 μL, shaked for 10 seconds and kept on incubation from 2 to 4 hours. The

fluorescence emission intensity of the samples were recorded by fluorimeter at λem = 590 nm (λex = 560 nm).

3.7 *In vitro* fluorescence and MR imaging uptake experiments in U87MG cells: For the *in vitro* targeting uptake experiments, about 2.5×10^5 U87MG cells were seeded in 6 cm diameter dishes. For fluorescence imaging, the cells were incubated with Gd-MSNs-RGD as targeting probes and Gd-MSNs-PEG as control at the concentration of 200 μg/mL, at 37 °C for 4 h. Fluorescence imaging was performed on the Leica TCS SP5 II laser confocal scanning microscopy system. A 60× oil-immersion objective lens was used. Excitation of DAPI was carried out with a semiconductor laser at 405 nm, and its emission was collected at 460±20 nm. For FITC images, λex = 488 nm and λem = 500–560 nm (scale bars = 75 μm) conditions were used. For MR imaging, the cells were incubated with Gd-MSNs-RGD and Gd-MSNs-PEG, respectively, at different Gd concentrations (5-20 μM) for 3 h at 37 °C. At the end of the incubation, cells were washed three times with 5 mL of ice-cold PBS, detached with trypsin/EDTA, and transferred into falcon tubes. MR images of cell pellets were acquired on a Bruker Avance300 (7T) instrument equipped with a micro-imaging probe. MR images were obtained by using a standard T_1-weighted multi-slice multi-echo sequence (TR/TE/NEX = 200:3.3:16, field of view = 1.2 cm, one slice = 1 mm). After imaging, the cell samples were collected and sonicated at 30% of power for 30 s in ice, and the total protein content was measured by the Bradford assay by using bovine serum albumin as standard (Biorad, Hercules, CA, USA).[33] Next, the reset cell samples were digested with concentrated HNO_3 (70%, 1 mL) under microwave heating (Milestone MicroSYNTH Microwave labstation). The Gd content in

the cell samples was determined by using inductively coupled plasma mass spectrometry (ICP-MS; element-2; Thermo-Finnigan, Rodano (MI), Italy).

3.8 Animal model: Balb/C nude mice (aged 6 weeks and weighted 18 - 22 g) were purchased from Harlan Laboratories. Handling and all manipulations were carried out in accordance with European Community guidelines, and all the experiments were approved by the Ethical Committee of the University of Turin. A suspension of 2×10^6 A431 cells in 0.1 mL DMEM medium without serum was subcutaneously injected in right flank of each female mouse. After 10 days, a suspension of 5×10^6 U87MG cells in 0.1 mL EMEM medium was subcutaneously injected in the left flank of the same female mouse. When both the tumors reached 0.4-0.6 cm in diameter, the tumour bearing mice were imaged.

3.9 *In vivo* MRI: *In vivo* MRI experiments with Gd-MSNs-PEG and Gd-MSNs-RGD were carried out on U87MG and A431 tumor xenografts in Balb/C mice (n = 6) with a 1T scanner (Bruker, Icon Instrument). The mice were anesthetized with isofluorane and placed in cradle with an infusion line placed in the tail vein for the nanoprobes administration. Each nanoprobe suspension was administered at the dose of 0.021 mmol/kg of Gd^{3+}. During measurements, respiration was monitored with a sensor connected to an ECG/respiratory unit.

After localization of the tumor with a T_2-weighted scan with spin–echo sequence (TR/TE = 3000/60 ms, number of averages (NA) = 4), serial T_1-weighted MR scans with multi-slice spin-echo sequence (TR/TE = 380/14 ms, number of averages (NA) = 4), were collected before the nanoprobes were intravenously injected and after 1, 6 and 24 hours. For the image analysis, the T_1 Contrast-to-Noise Ratio ($CNR(T_1)$) was measured as follows:

$$CNR\ T_1 = \frac{SI_{(A)} - SI_{(B)}}{SDV_{(B)}}$$

Where $SI_{(A)}$ is the MRI signal intensity of a given ROI, $SI_{(B)}$ is the signal from the background and $SDV_{(B)}$ is the standard deviation of the signal noise of background. Values reported are expressed as CNR(T_1) %, which correlates CNR(T_1) POST-contrast to the corresponding pre-contrast value.

3.10 Ex vivo Fluorescence Microscopy Analysis: After *in vivo* MR imaging, the fluorescence microscopy analysis of the major organs of both control and target groups were carried out by the Fluorescence microscope AXIO ZOOM.VI16 (ZEISS, Germany) to investigate the biodistribution of the injected particles (FITC excitation 470±20 nm, emission 525±25 nm, Exposition 170 ms, Gain 120, Zoom 4X). A control mouse without injection of any contrast agent was used for the analogous fluorescence images as blank.

4 Conclusion

In summary, a RGD-labeled multifunctional nanoprobe targeting integrin $\alpha_V\beta_3$ receptors based on modified MSNs has been synthesized and tested both *in vitro* (fluorescence/MRI) and *in vivo* (MRI). The small size (~ 30 nm) and good monodispersity (PDI < 0.05) endow these MSNs with excellent physiological stability and biocompatibility. Further surface modification endows them with high relaxivity (37.6 $mM^{-1}s^{-1}$ at 21.5 MHz) and targeting capability. The application of integrin $\alpha_v\beta_3$ targeted Gd-MSNs-RGD for high sensitive multifunctional imaging study, from the cellular scale to small-animal whole-body evaluation, has been demonstrated This study may open new perspectives for the design of high sensitivity multimodal nanotherapeutics for application in cancer diagnosis and management as well as in imaging-guided surgery and therapy.

Supporting information:

Absorption and emission spectra, Energy dispersive x-ray analysis (EDXA) and XPS spectra, TGA, zeta-potential and the molecular structures of the Gd-complexes which have been cited.

Acknowledgments

This research was supported by a Marie Curie International Incoming Fellowship within the 7th European Community Framework Programme (PIIF-GA-2011-298821). MIUR (Grant PRIN 2012SK7ASN), AIRC (Investigator Grant IG 14565), CIRCMSB and Compagnia di San Paolo are also gratefully acknowledged.

References

1. E. Terreno, D. D. Castelli, A. Viale and S. Aime, *Chem. Rev.*, 2010, **110**, 3019-3042.
2. K. N. Raymond and V. C. Pierre, *Bioconjugate Chem.*, 2004, **16**, 3-8.
3. F. Carniato, L. Tei, M. Cossi, L. Marchese and M. Botta, in *Chem. Eur. J.*, 2010, 16, 10727–10734.
4. P. Caravan, *Chem. Soc. Rev.*, 2006, **35**, 512-523.
5. C.-H. Huang, K. Nwe, A. Al Zaki, M. W. Brechbiel and A. Tsourkas, *ACS Nano*, 2012, **6**, 9416–9424.
6. G. Ratzinger, P. Agrawal, W. Koner, J. Lonkai, H. M. H. F. Sanders, E. Terreno, M. Wirth, G. J. Strijkers, K. Nicolay and F. Gabor, *Biomaterials*, 2010, **31** 8716-8723.
7. R. N. Mariano, D. Alberti, J. C. Cutrin, S. Geninatti Crich and S. Aime, *Mol. Pharmaceutics*, 2014, **11**, 4100–4106.
8. M. A. Bruckman, K. Jiang, E. J. Simpson, L. N. Randolph, L. G. Luyt, X. Yu and N. F. Steinmetz, *Nano Lett.*, 2014, **14**, 1551-1558.

9. Y. Song, X. Y. Xu, K. W. MacRenaris, X. Q. Zhang, C. A. Mirkin and T. J. Meade, in *Angew. Chem. Int. Ed.* , 2009, 48, 9143–9147.

10. F. Carniato, L. Tei, A. Arrais, L. Marchese and M. Botta, *Chem. Eur. J.*, 2013, **19**, 1421-1428.

11. C.-P. Tsai, Y. Hung, Y.-H. Chou, D.-M. Huang, J.-K. Hsiao, C. Chang, Y.-C. Chen and C.-Y. Mou, *Small*, 2008, **4**, 186-191.

12. T. Lammers, S. Aime, W. E. Hennink, G. Storm and F. Kiessling, *Acc. Chem. Res.*, 2011, **44**, 1029-1038.

13. L. Y. Rizzo, B. Theek, G. Storm, F. Kiessling and T. Lammers, *Curr. Opin. Bio.*, 2013, **24**, 1159–1166.

14. D. Tarn, C. E. Ashley, M. Xue, E. C. Carnes, J. I. Zink and C. J. Brinker, *Acc. Chem. Res.*, 2013, **46**, 792–801.

15. Y.-S. Lin, K. R. Hurley and C. L. Haynes, *J. Phys. Chem. Lett.*, 2012, **3**, 364-374.

16. K. Ma, H. Sai and U. Wiesner, *J. Am. Chem. Soc.*, 2012, **134**, 13180-13183.

17. J. A. Barreto, W. O'Malley, M. Kubeil, B. Graham, H. Stephan and L. Spiccia, *Adv. Mater.*, 2011, **23**, H18–H40.

18. X. Chen, *Mini Rev. Med. Chem.*, 2006, **6**, 227-233.

19. L. An, H. Hu, J. Du, J. Wei, L. Wang, H. Yang, D. Wu, H. Shi, F. Li and S. Yang, *Biomaterials*, 2014, **35** 5381-5392.

20. G. Mondal, S. Barui and A. Chaudhuri, *Biomaterials*, 2013, **34**, 6249-6260.

21. R. Weissleder, M. Nahrendorf and M. J. Pittet, *Nat Mater*, 2014, **13**, 125-138.

22. Q. Zhang, X. Wang, P.-Z. Li, K. T. Nguyen, X.-J. Wang, Z. Luo, H. Zhang, N. S. Tan and Y. Zhao, *Adv. Funct. Mater.*, 2014, **24**, 2450–2461.

23. L. K. Bogart, G. Pourroy, C. J. Murphy, V. Puntes, T. Pellegrino, D. Rosenblum, D. Peer and R. Lévy, *ACS Nano*, 2014, **8**, 3107–3122.

24. Y.-S. Lin, N. Abadeer, K. R. Hurley and C. L. Haynes, *J. Am. Chem. Soc.*, 2011, **133**, 20444-20457.

25. J. C. Groen, L. A. A. Peffer and J. Pérez-Ramírez, *Microporous Mesoporous Mater.*, 2003, **60**, 1-17.

26. H. Hu, H. Zhou, J. Liang, L. An, A. Dai, X. Li, H. Yang, S. Yang and H. Wu, *J. Colloid Interface Sci.*, 2011, **358**, 392-398.

27. A. Abdukayum, C.-X. Yang, Q. Zhao, J.-T. Chen, L.-X. Dong and X.-P. Yan, *Anal. Chem.*, 2014, **86**, 4096-4101.

28. A. T. Preslar, G. Parigi, M. T. McClendon, S. S. Sefick, T. J. Moyer, C. R. Haney, E. A. Waters, K. W. MacRenaris, C. Luchinat, S. I. Stupp and T. J. Meade, *ACS Nano*, 2014, **8**, 7325–7332.

29. P. Caravan, J. J. Ellison, T. J. McMurry and R. B. Lauffer, *Chem. Rev.*, 1999, **99**, 2293-2352.

30. F. Kielar, L. Tei, E. Terreno and M. Botta, *J. Am. Chem. Soc.*, 2010, **132**, 7836-7837.

31. K. Zhang, L.-L. Xu, J.-G. Jiang, N. Calin, K.-F. Lam, S.-J. Zhang, H.-H. Wu, G.-D. Wu, B. Albela, L. Bonneviot and P. Wu, *J. Am. Chem. Soc.*, 2013, **135**, 2427-2430.

32. E. Gianolio, C. Cabella, S. Colombo Serra, G. Valbusa, F. Arena, A. Maiocchi, L. Miragoli, F. Tedoldi, F. Uggeri, M. Visigalli, P. Bardini, S. Aime, *J. Biol. Inorg. Chem.*, 2014, **19**, 719-726.

33. M. M. Bradford, *Anal. Biochem.,* 1976, **72**, 248-254.